Chemical Science



EDGE ARTICLE

View Article Online
View Journal | View Issue



Cite this: Chem. Sci., 2019, 10, 8129

dll publication charges for this article have been paid for by the Royal Society of Chemistry

Received 8th April 2019 Accepted 3rd July 2019

DOI: 10.1039/c9sc01686d

rsc.li/chemical-science

A sterically hindered asymmetric D-A-D' thermally activated delayed fluorescence emitter for highly efficient non-doped organic light-emitting diodes†

Zhan Yang,‡^a Zhu Mao, (1)‡^a Chao Xu,^b Xiaojie Chen,^a Juan Zhao, (1)*^a Zhiyong Yang,^a Yi Zhang, (1)*^a William Wu,^c Shibo Jiao,^c Yang Liu,^c Matthew P. Aldred^a and Zhenguo Chi (1)*^a

Thermally activated delayed fluorescence (TADF) materials have opened a new chapter for high-efficiency and low-cost organic light-emitting diodes (OLEDs). Herein, we describe a novel and effective design strategy for TADF emitters which includes introducing a carbazole donor unit at the *ortho*-position, at which the donor and acceptor groups are spatially in close proximity to guarantee the existence of intramolecular electrostatic attraction and through-space charge transfer, leading to reduced structural vibrations, suppressed non-radiative decay and rapid radiative decay to avoid excited state energy loss. As a result, a green TADF emitter (2Cz-DPS) showing high solid-state photoluminescence quantum efficiency (91.9%) and excellent OLED performance was produced. Theoretical simulations reveal that the non-adiabatic coupling accelerates the reverse intersystem crossing of 2Cz-DPS, resulting in a state-of-the-art non-doped OLED with an extremely high external quantum efficiency of 28.7%.

Introduction

Organic-based emissive materials that exhibit thermally activated delayed fluorescence (TADF) properties can harvest both singlet and triplet excitons for light emission *via* reversible intersystem crossing (RISC) from the lowest triplet (T₁) to singlet (S₁) excited states, leading to a maximum internal quantum efficiency (IQE) of electroluminescence of 100%. Accordingly, fully utilizing the TADF mechanism in "thirdgeneration" organic light-emitting diodes (OLEDs) has attracted considerable attention.¹ TADF-based emitters are composed of donor (D) and acceptor (A) groups in various structural configurations which help to achieve a small overlap between the highest occupied molecular orbital (HOMO) and lowest unoccupied molecular orbital (LUMO), reducing the spin exchange

energy (I) which ultimately leads to a small energy gap between the S_1 and T_1 (ΔE_{ST}), which facilitates the RISC process. However, linear D-A linkages tend to decrease the radiative transition oscillator strength (f) and induce intramolecular D-A rotation and other vibrational modes of the excited-state molecules that dissipate energy. These internal motions can be reduced by introducing large steric hindrance between the D and A units, which can not only restrict non-radiative pathways,2 but also enable rapid radiative decay from the excitedstate molecules,3 leading to high-efficiency TADF emitters. In general, high-performance TADF-OLEDs are fabricated by dispersing the TADF emitters into host materials to alleviate exciton annihilation,4 leading to issues such as complicated fabrication processes and possible host-guest phase separation. Therefore, the non-doping technique, which enables ease of fabrication along with more reliable and reproducible output manufacturing of the fabricated devices, is more attractive. Accordingly, aggregation-induced emission (AIE) materials are ideal for utilization as non-doped emissive layers (EMLs) due to their unusually strong fluorescence in the "aggregate-state" (film state).5 In this regard, in 2014 we proposed a structural design strategy that involved the merging of the two concepts, AIE and TADF, together in one molecule.

Inserting an electron accepting sulfonyldibenzene core in between carbazole and phenothiazine electron donating units afforded an asymmetric TADF material with outstanding near-quantitative solid-state photoluminescence quantum yield (PLQY) (97.3%). Thereafter, this strategy has been validated many times towards the exploration of efficient TADF emitters

PCFM Lab, GDHPPC Lab, Guangdong Engineering Technology, Research Center for High-performance Organic and Polymer Photo-electric, Functional Films, State Key Laboratory of OEMT, School of Chemistry, Sun Yat-Sen University, Guangzhou 510275, China. E-mail: zhaoj95@mail.sysu.edu.cn; ceszy@mail.sysu.edu.cn; chizhg@mail.sysu.edu.cn

^bKey Laboratory of Theoretical Chemistry of Environment, Ministry of Education, School of Chemistry & Environment, South China Normal University, Guangzhou 510006. PR China

R&D Center, Shenzhen China Star Optoelectronics Semiconductor Display Technology Co., Ltd., Shenzhen 518132, China

 $[\]dagger$ Electronic supplementary information (ESI) available. CCDC 1891672. For ESI and crystallographic data in CIF or other electronic format see DOI: 10.1039/c9sc01686d

[‡] Dr Z. Yang and Dr Z. Mao contributed equally to this work.

Chemical Science Edge Article

and fabrication of non-doped OLEDs⁷ and can achieve very good OLED performance, such as an external quantum efficiency (EQE) \sim 20%. Despite these advances, there are still no reports regarding TADF emitters that provide non-doped OLEDs with EQEs close to 30%, which is the upper limit of common bottomemitting OLEDs.

In this work, we present a novel and effective structural design strategy for TADF emitters with strong solid-state emission properties, wherein D and A groups are linked at the *ortho*-position to afford a spatially close D–A interaction, leading to reduced vibrations and suppressed non-radiative pathways. In addition, **2Cz-DPS** possesses dual-charge transfer pathways (through-bond charge transfer and through-space charge transfer), resulting in rapid prompt and delayed decay. Significantly, the designed asymmetric TADF emitter **2Cz-DPS** with a highly twisted conformation exhibits a high PLQY as a neat film (AIE property) and excellent solid-state thermal stability. Most importantly, **2Cz-DPS** affords a record-high EQE of 28.7% amongst other reported non-doped OLEDs.

Results and discussion

Molecular design strategy and theoretical simulations

2Cz-DPS is derived from our previously reported compound 4Cz-DPS, in which the carbazole group has been relocated to the ortho-position as opposed to the original para-position. The molecular structures of 4Cz-DPS and 2Cz-DPS based on the carbazole and phenothiazine donor groups and the diphenylsulfone acceptor group are illustrated in Fig. 1, in which 4Cz-DPS was synthesized according to our previous report⁶ and 2Cz-DPS was synthesized in three steps (Scheme S1 in the ESI†) using cheap and common reagents. Structural characterization was conducted by ¹H NMR, ¹³C NMR, EI-MS and HRMS (Fig. S1-S9, ESI†) and single crystal analysis. Similar to AIE-active 4Cz-**DPS**, **2Cz-DPS** with a highly twisted conformation also possesses AIE properties (more details are shown in Fig. S10, ESI†). The THF/water solutions of 2Cz-DPS with low water fractions show very weak emission, while highly intense green emission is observed when a large amount of water ($f_w = 90\%$) is added (Fig. S10a†), and nanoaggregates with effective diameters of 186 nm are evidenced by dynamic light scattering study

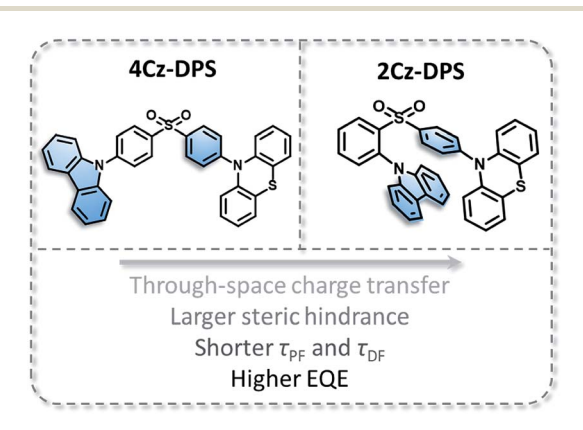


Fig. 1 Molecular structures of 4Cz-DPS and 2Cz-DPS

(Fig. S10b†). Moreover, **2Cz-DPS** has a PLQY of only 0.9% even in dilute non-polar hexane, which excludes the polarity quenching of the charge transfer (CT) emitters in the solution state, while the PLQY is greatly enhanced to 91.9% in the solid state. These results indeed demonstrate that **2Cz-DPS** is AIE active.

As demonstrated from the conformation in the single crystal of 2Cz-DPS (Fig. 2a), the carbazole donor group is nearly parallel to the phenyl ring attached to the diphenyl-sulfone acceptor group with a co-facial alignment at a distance of 3.1-3.8 Å and a tilt angle (θ) of 14.23°, suggesting strong intramolecular interactions between D and A. On the other hand, the single crystal structure of 4Cz-DPS (Fig. S11a, ESI†) demonstrates orthotropic attachment between the carbazole group and the diphenyl-sulfone group. To reveal the intramolecular non-covalent interactions in 2Cz-DPS, the functions of reduced density gradient (RDG) and Sign $(\lambda_2)\rho$ were calculated using Multiwfn software. 10 RDG analysis (Fig. 2b and c) confirms the presence of obvious intramolecular attractive interactions (green region) and larger steric hindrance (brown region) between D and A segments in 2Cz-DPS, which could effectively restrict the intramolecular vibrations and prevent energy loss of the excited molecules. In contrast, the linearly linked conformation of 4Cz-DPS exhibits weak intramolecular interactions (Fig. 2d), which is a common phenomenon found in general TADF molecules. According to time-dependent density functional theory (TD-DFT) calculations based on the conformations extracted from single crystal analysis, the HOMOs are mainly distributed on the phenyl-phenothiazine or carbazole units (D), while the LUMO is mostly located on the diphenyl-

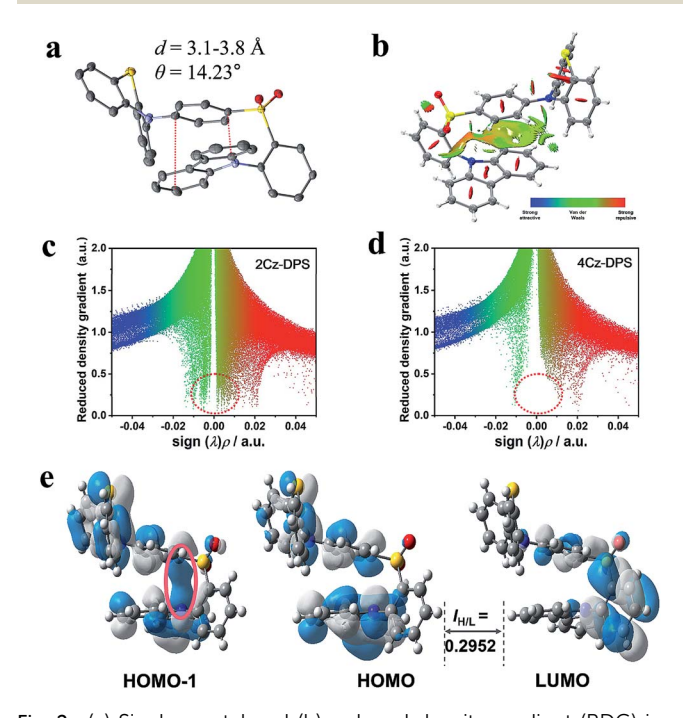


Fig. 2 (a) Single crystal and (b) reduced density gradient (RDG) isosurface map with an isovalue of 0.5 for 2Cz-DPS. The functions of RDG and Sign (λ_2) ρ for (c) 2Cz-DPS and (d) 4Cz-DPS. (e) HOMO and LUMO distribution of 2Cz-DPS, showing the overlap integral extents $I_{H/L}$.

Table 1 Summary of photo-physical and thermal properties of 2Cz-DPS and 4Cz-DPS neat films

TADF	λ_{A}^{a} (nm)	$\lambda_{\rm A}^{a} \left({\rm nm} \right) \hspace{0.5cm} \lambda_{\rm PL}^{b} \left({\rm nm} \right) \hspace{0.5cm} T_{\rm d}^{c} \left({}^{\circ} {\rm C} \right) \hspace{0.5cm} T_{\rm g}^{d} \left({}^{\circ} {\rm C} \right) \hspace{0.5cm} \phi_{\rm PF}^{e}$	$T_{ m d}^{c}(^{\circ}{ m C})$	$T_{\mathrm{g}}^{\ d}\left({}^{\circ}\mathrm{C}\right)$	$\phi_{ ext{PF}}^{e}$ (%)	$\phi_{\mathrm{DF}}^{f}(\%)$	$ au_{ ext{PF}}^g ext{(ns)}$	$ au_{\mathrm{DF}}^{h}\left(\mu\mathrm{s}\right)$	$k_{\mathrm{ISC}}^{i}\left(\mathrm{s}^{-1}\right)$	$k_{\mathrm{RISC}}^{j}\left(\mathrm{s}^{-1}\right)$	$\Delta E_{\mathrm{ST}}^{}k}\left(\mathrm{eV} ight)$	$\Delta E_{\mathrm{ST}}^{\ \ l}\left(\mathrm{eV} ight)$	$(\%) \phi_{\mathrm{DF}}^{f}\left(\%\right) \tau_{\mathrm{PF}}^{g}\left(\mathrm{ns}\right) \tau_{\mathrm{DF}}^{h}\left(\mu\mathrm{s}\right) k_{\mathrm{ISC}}^{i}\left(\mathrm{s}^{-1}\right) k_{\mathrm{RISC}}^{f}\left(\mathrm{s}^{-1}\right) \Delta E_{\mathrm{ST}}^{k}\left(\mathrm{eV}\right) \Delta E_{\mathrm{ST}}^{l}\left(\mathrm{eV}\right) \mathrm{PLQY}^{m}\left(\%\right) E_{\mathrm{g}}^{g}\left(\mathrm{eV}\right) \Delta E_{\mathrm{ST}}^{g}\left(\mathrm{eV}\right) $	$E_{\rm g}^{\ n}\left({ m eV}\right)$
4Cz-DPS	326	530	394	121	17.5	79.8	6.3	62.2	2.28×10^7	2.28×10^7 0.89×10^5 0.25	0.25	0.35	97.3	2.2
2Cz-DPS 341	341	520	389	111	26.7	65.2	4.4	19.1	4.31×10^7	4.31×10^7 1.74×10^5 0.32	0.32	0.41	91.9	2.5
^a Absorpti of delayed	on peak. b PL emission. g	, emission pea Prompt fluore	ık. [¢] Temper escence lifet	ature of ther	mal decomp	osition at 5% /ed fluoresce	weight loss nce lifetime	. ^d Glass-tran component.	isition tempera i Rate constan	ture. ^e Quantur t of ISC for trij	n efficiency of plet excited st	prompt emiss ates. ^j Rate co	^a Absorption peak. ^b PL emission peak. ^c Temperature of thermal decomposition at 5% weight loss. ^d Glass-transition temperature. ^e Quantum efficiency of prompt emission. ^f Prompt fluorescence lifetime component. ^h Delayed fluorescence lifetime component. ^e Rate constant of ISC for triplet excited states. ^f Rate constant of RISC for triplet	efficiency for triplet

quantum yield measured under JA " excited states. * S₁ and T₁ energy difference determined from experiments. 'S₁ and T₁ energy difference determined from theoretical simulations. vacuum." Energy gap calculated from the onset of absorption spectra sulfone core (A) of the 4Cz-DPS and 2Cz-DPS compounds (Fig. 2e and S11b†). Interestingly, as observed from the HOMO-1 of 2Cz-DPS, there is an obvious orbital overlap between the parallel carbazole and phenyl planes, confirming the through-space charge transfer characteristics between D and A.11 Due to the close proximity between D and A in 2Cz-DPS, intramolecular charge transfer occurs not only through the molecular conjugated backbone, but also by through-space conjugation mediated by intramolecular D-A interactions. 11b,12 The dual charge transfer pathways greatly enhance the oscillator strength (f = 0.0207) for faster radiative decay, in comparison to the isomer 4Cz-DPS (f =0.0074). As a result, the strong intramolecular interactions generated in 2Cz-DPS help to increase the molecular rigidity, decrease the relaxation of the excited states, and enhance the radiative transition rate,3 which can also be evidenced from shortened transient and delayed lifetimes (Fig. S12, ESI†), thus facilitating the occurrence of efficient TADF. The charge transfer (CT) character can also be verified from the large Stokes shift with increasing solvent polarity (Fig. S13 and S14, ESI†).13 When the solvent polarity is increased from *n*-hexane to DMF, the PL spectral peaks are red-shifted from 475 nm to 565 nm for 4Cz-DPS and from 471 nm to 567 nm for 2Cz-DPS (Fig. S13†), while their absorption spectra are relatively insensitive to the solvent polarity (Fig. S14†). In contrast to the solutions showing dual emission, the 4Cz-DPS and 2Cz-DPS films give structure-less PL spectra (Fig. S15, ESI†), due to the highly strengthened and dominant intermolecular CT process in the solid-sate films.14

TADF property characterization

Temperature dependent steady-state spectra of the 2Cz-DPS film from 17 to 298 K (Fig. S16a, ESI†) show that the emission intensity gradually increases as the temperature rises. Furthermore, transient PL spectra of the 2Cz-DPS film were measured (Fig. S16b, ESI†) and display two-component decays, including the prompt and the delayed components. With increasing temperature from 17 to 298 K, the delayed component progressively increases, leading to prompt and delayed lifetimes of 4.4 ns and 19.1 µs for 2Cz-DPS at 298 K, respectively, and 6.3 ns and 62.2 μs for 4Cz-DPS, respectively (Fig. S17, ESI†). The photo-physical properties of the TADF materials are summarized in Table 1. Therefore, when the substitution position changes from para- to ortho-, 2Cz-DPS shows both faster prompt decay and delayed decay at room temperature, which is quite essential for high-performance TADF-based OLEDs.¹⁵ Therefore, the steady-state spectra and transient PL spectra results confirm the TADF nature of 2Cz-DPS.

The TADF feature is further demonstrated by oxygensensitive PL spectra (Fig. S18, ESI†). In contrast to those under air conditions, the lifetimes of the delayed components in a vacuum are increased, confirming that the T₁ excitons of the TADF compounds can be deactivated by oxygen.¹⁶ It is noteworthy that the PLQYs of 4Cz-DPS and 2Cz-DPS films in air were measured to be 74.7% and 65.3%, respectively, while their PLQYs in a vacuum reach up to 97.3% and 91.9%, respectively, resulting from the reduction of oxygen quenching of the delayed component. The $\Delta E_{\rm ST}$ of the 4Cz-DPS and 2Cz-DPS films was calculated from their fluorescence

phosphorescence spectra (Fig. S19, ESI†),¹⁷ and estimated to be 0.25 and 0.32 eV, respectively, which are relatively large values amongst other recently reported TADF emitters.¹ As seen from the crystal of **2Cz-DPS** and **4Cz-DPS**, the axial conformation of phenothiazine accounts for the large $\Delta E_{\rm ST}$ of the compounds.¹⁸ Compared to **4Cz-DPS**, **2Cz-DPS** with through-space charge transfer features possessed a slightly enlarged $\Delta E_{\rm ST}$ which can be ascribed to the larger overlap integral of the HOMO and LUMO ($I_{\rm H/L}=0.2952$, Fig. 1e).^{8a} This is in contrast with previously reported through-space charge transfer TADF emitters in which through-space D–A interaction minimizes the electron-exchange energy and induces a narrow $\Delta E_{\rm ST}$.¹⁹ However, the

larger overlap integral of frontier orbitals increases the transi-

tion dipole moment and thus results in a faster prompt decay.

Non-adiabatic coupling effect

Chemical Science

In order to evaluate the origin of the faster delayed decay in 2Cz-DPS, natural transition orbital (NTO) simulations on both 2Cz-DPS and 4-CzDPS were performed to provide insight into the transition features of the excited states. A clear CT character of the lowest S₁ is expected and a strong locally excited (LE) nature of the lowest T₁ is observed (Fig. S20 and S21, ESI†), which can also be demonstrated by the vibronic phosphorescence emission at 77 K. In general, the RISC process is driven by first-order spin-orbit coupling (SOC) in this type of TADF emitter (3LE as the lowest triplet state).20 In our asymmetric D-A-D' systems, especially 2Cz-DPS, the ΔE_{ST} and SOC matrix element value of S₁ and T₁ are 0.41 eV and 0.17 cm⁻¹ (Fig. 3), respectively, too large for the occurrence of efficient RISC according to the Fermi golden rule. However, 2Cz-DPS with a larger ΔE_{ST} and smaller SOC constant $\xi(S_1, T_1)$ exhibits a much shorter delayed lifetime $(\tau_{DF}, 19.1 \mu s)$ than para-substituted 4Cz-DPS (62.2 μs), indicating a faster RISC. This abnormal phenomenon implies that another factor causes the acceleration process. Further analysis of the NTO pairs reveals that several triplet states exist below the S₁ energy level. In 2Cz-DPS, these upper triplet states exhibit different electronic configurations. T₁ and T₃ show significant LE characteristics, while T2, T4 and T5 show weak CT characteristics. These dark excited triplet states have been regarded to play an important role and can result in a second order coupling (non-adiabatic coupling) of the excited states which leads to a complete understanding of the rapid RISC process, especially in TADF emitters with a large ΔE_{ST} .²² The gap between T₂ (CT)

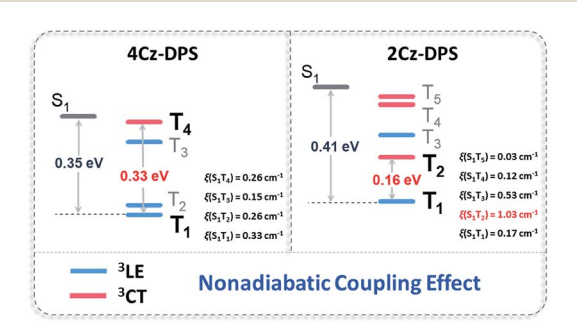


Fig. 3 Energy level diagrams, spin-orbital coupling constants (ξ) and non-adiabatic coupling effects of 4Cz-DPS and 2Cz-DPS.

and T₁ (LE) is 0.16 eV in 2Cz-DPS, and it is 0.33 eV in 4Cz-DPS between T₄ (CT) and T₁ (LE). As reported before, the reversible energy transfer between the lowest 3LE and upper 3CT is considered as a fast intramolecular-electron exchange within a 0.2 eV gap.²³ Therefore, the narrower gap between the ³CT and ³LE contributes to a faster T₁-T₂ equilibrium (or reverse internal conversion) by non-adiabatic coupling, resulting in a strong mixing of triplet states,24 which then gives rise to a higher RISC rate (k_{RISC}) in **2Cz-DPS** of $1.74 \times 10^5 \text{ s}^{-1}$, which is more than twice higher than that in **4Cz-DPS** $(0.89 \times 10^5 \text{ s}^{-1})$. Additionally, the SOC constant (ξ) of 2Cz-DPS between S₁ and T₂ calculated by TD-DFT is 1.03 cm⁻¹, suggesting an effective RISC, which is consistent with the shorter $\tau_{\rm DF}$. Therefore, not only does $\Delta E_{\rm ST}$ control the RISC process, but the non-adiabatic coupling between the triplet CT and LE also plays a key role in rapid RISC in 2Cz-DPS, leading to the shortened $\tau_{\rm DF}$. ²⁵ Compounds with shortened τ_{DF} have vast potential for highly efficient OLEDs.²⁶

Electrochemical and thermal properties

The electrochemical behavior of the compounds was examined by cyclic voltammetry (Fig. S22a†). The HOMO levels of **4Cz-DPS** and **2Cz-DPS** were determined to be 5.2 and 5.3 eV, respectively, and the bandgaps (E_g) of **4Cz-DPS** and **2Cz-DPS** were calculated to be 2.7 eV, from the onset of their absorption spectra in DCM solution with a concentration of 5×10^{-4} mol L⁻¹ (Fig. S22b†). Then, the LUMO levels of **4Cz-DPS** and **2Cz-DPS** were estimated to be 2.6 and 2.5 eV, respectively. As demonstrated by thermogravimetric analysis (TGA) and differential scanning calorimetry (DSC) (Fig. S23, ESI†), **4Cz-DPS** and **2Cz-DPS** exhibit high thermal stability with decomposition temperatures (T_d : corresponding to 5% weight loss) of 394 and 389 °C and glass transition temperatures (T_g) of 121 and 111 °C, respectively,

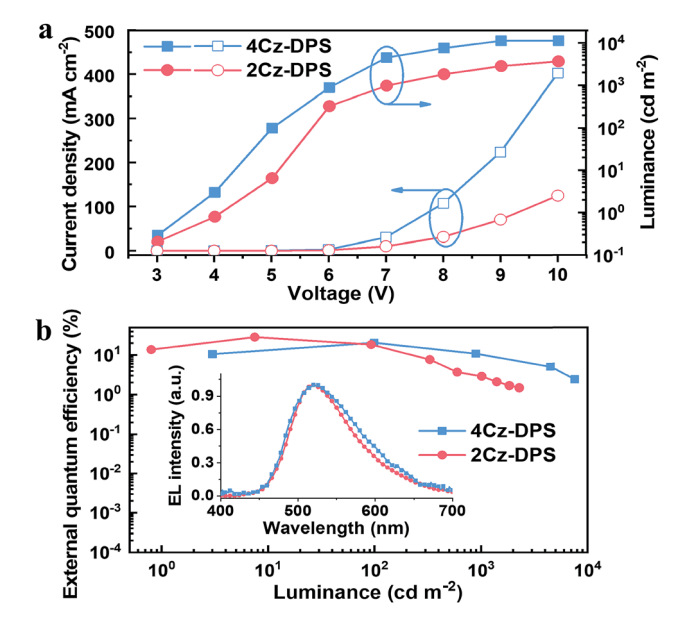


Fig. 4 (a) Current density-voltage-luminance and (b) external quantum efficiency-luminance curves of 4Cz-DPS and 2Cz-DPS devices. Inset: normalized EL spectra.

Edge Article Chemical Science

Table 2 EL performance of the non-doped OLEDs based on 4Cz-DPS and 2Cz-DPS

Device	$V_{\mathrm{on}}{}^{a}\left[\mathbf{V}\right]$	Luminance ^b [cd m ⁻²]	$\mathrm{EQE/CE/PE}^{c}\left[\%/\mathrm{cd}\;\mathrm{A}^{-1}/\mathrm{lm}\;\mathrm{W}^{-1}\right]$	$\mathrm{EQE/CE/PE}^{d}\left[\%/\mathrm{cd}\;\mathrm{A}^{-1}/\mathrm{lm}\;\mathrm{W}^{-1}\right]$	$\lambda_{\mathrm{EL}}^{e} [\mathrm{nm}]$	FWHM ^f [nm]
4Cz-DPS	3.5	11 310	20.7/61.2/38.4	14.6/53.1/32.5	524	108
2Cz-DPS	4.1	4220	28.7/82.3/51.8	8.4/28.8/15.6	518	96

^a Turn-on voltage at a luminance of 1 cd m⁻². ^b Maximum luminance. ^c Maximum efficiency. ^d Efficiency achieved at 300 cd m⁻². ^e EL peak wavelength. f Full-width-at-half-maximum.

which are beneficial for maintaining stable film morphology during device operation.

Non-doped OLED characterization

Electroluminescence (EL) properties of 4Cz-DPS and 2Cz-DPS were studied using neat EML films, and non-doped OLEDs were constructed with the device configuration ITO/PEDOT:PSS (30 nm)/m-bis(N-carbazolyl)benzene (MCP) (20 nm)/EML (30 nm)/ 1,3,5-tris(N-phenylbenzimidazol-2-yl)benzene (TPBI) (40 nm)/ LiF(1 nm)/Al (100 nm), wherein EML = 4Cz-DPS or 2Cz-DPS. The EL performance is shown in Fig. 4 and summarized in Table 2. With regard to the non-doped 4Cz-DPS device, the maximum EQE, current efficiency (CE) and power efficiency (PE) are obtained to be 20.7%, 61.2 cd A⁻¹ and 38.4 lm W⁻¹, respectively, at a luminance of 100 cd m⁻², which to the best of our knowledge are amongst the best performances of non-doped TADF-OLEDs.²⁷ Surprisingly, the non-doped 2Cz-DPS device achieves a maximum EQE, CE and PE of 28.7%, 82.3 cd A^{-1} and 51.7 lm W^{-1} , respectively, at a luminance of 10 cd m⁻², without the use of any light out-coupling methods. The EL spectra (inset of Fig. 4b) with peaks at 524 nm and 516 nm correspond to the emission of 4Cz-DPS and 2Cz-DPS, respectively. Furthermore, five more 2Cz-DPS devices were implemented and showed maximum EQEs ranging from 24.8% to 30.4% (Fig. S24, ESI†), thus confirming good efficiency reproducibility of the 2Cz-DPS devices. The high EQE value of the 2Cz-DPS containing device confirms the state-of-theart performance of non-doped TADF-OLEDs,7,8 and is even comparable to that of the best performing doped OLEDs based on TADF or phosphorescence-based emitters.28 As shown by the results of single carrier devices (Fig. S25, ESI†), 2Cz-DPS shows a reduced electron mobility compared to 4Cz-DPS, due to the presence of a bulky substituent in 2Cz-DPS preventing charge transport and suppressing intermolecular interactions by larger steric hindrance.29 Importantly, more balanced hole- and electron-mobilities are observed for 2Cz-DPS than for 4Cz-DPS, which benefits the higher charge-carrier balance in the 2Cz-DPS device, and hence higher efficiencies. Despite this, the 2Cz-DPS device shows a relatively high efficiency roll-off compared to the 4Cz-DPS device, as high charge-carrier balance features alone cannot guarantee a low efficiency roll-off. It can also be observed from single carrier devices that the electron mobility of 4Cz-DPS is much higher than its hole mobility; thus the recombination zone (RZ) in the 4Cz-DPS device is confined in the EML but toward the HTL/EML interface. On the other hand, the hole mobility of 2Cz-DPS is slightly higher than its electron mobility, suggesting movement of the RZ toward the EML/ETL interface in the 2Cz-DPS device, which can induce efficiency roll-off.30 In addition, the reduced self-quenching of the 4Cz-DPS emitter, as

evidenced by the higher PLQY of the 4Cz-DPS film than of the 2Cz-DPS film, could also be responsible for the lower efficiency roll-off in the 4Cz-DPS device.4a We further investigate the efficiency roll-off behaviours by taking both triplet-triplet annihilation (TTA) and singlet-polaron annihilation (SPA) into account, which are assumed to be dominant in TADF-based OLEDs.31 As seen in Fig. S26,† the main origin for efficiency roll-off in the 2Cz-**DPS** device is TTA (especially at high current density), while it is SPA in the 4Cz-DPS device, which is in good agreement with the results from 4Cz-DPS based single carrier devices showing abundant and imbalanced charge carriers (Fig. S25b†).

Conclusions

In summary, an ortho-substituent design strategy promoting steric hindrance has afforded excellent AIE-TADF emitters, and highefficiency TADF-OLEDs have been subsequently demonstrated. The intramolecular interactions between the spatially close donor and acceptor moieties suppress structural vibrations, prevent the excited state energy loss and generate space conjugation. The dual intramolecular charge transfer pathways including through-bond charge transfer and through-space charge transfer enhance the radiative transition oscillator strength and accelerate the prompt decay. Although the ΔE_{ST} of 2Cz-DPS is increased by orthosubstitution, a faster delayed decay is obtained with the assistance of non-adiabatic coupling. The designed compound 2Cz-DPS exhibits high solid-state PLQY and good thermal stability in the thin film state. Most significantly, 2Cz-DPS endows the TADF-OLEDs with outstanding performance such as a record-high EQE of 28.7% by adopting a non-doped EML system. These results confirm that the presented design strategy opens up new possibilities to develop highly efficient TADF emitters and devices.

Conflicts of interest

There are no conflicts to declare.

Acknowledgements

This work was financially supported by the National Natural Science Foundation of China (NSFC: 51733010, 61605253, 21672267 and 51603232), Science and Technology Planning Project of Guangdong (2015B090913003 and 2015B090915003), Guangdong Natural Science Funds for Distinguished Young Scholars (2017B030306012), China Postdoctoral Science Foundation (2017M620395), Fundamental Research Funds for the Central Universities, and Shenzhen China Star Optoelectronics Semiconductor Display Technology Co., Ltd. (CSOT). We thank Chung-Chih Wu (National Taiwan University) for performing UV-vis absorption and phosphorescence spectra measurements for the TADF materials.

References

Chemical Science

- Z. Y. Yang, Z. Mao, Z. L. Xie, Y. Zhang, S. W. Liu, J. Zhao,
 J. R. Xu, Z. G. Chi and M. P. Aldred, *Chem. Soc. Rev.*, 2017,
 46, 915–1016.
- 2 D. Zhang, M. Cai, Y. Zhang, D. Zhang and L. Duan, *Mater. Horiz.*, 2016, 3, 145–151.
- 3 (a) J. S. Ward, R. S. Nobuyasu, A. S. Batsanov, P. Data, A. P. Monkman, F. B. Dias and M. R. Bryce, *Chem. Commun.*, 2016, 52, 2612–2615; (b) H.-J. Park, S. H. Han and J. Y. Lee, *J. Mater. Chem. C*, 2017, 5, 12143–12150.
- 4 (*a*) T.-L. Wu, M.-J. Huang, C.-C. Lin, P.-Y. Huang, T.-Y. Chou, R.-W. Cheng, H.-W. Lin, R.-S. Liu and C.-H. Cheng, *Nat. Photonics*, 2018, **12**, 235–240; (*b*) T.-A. Lin, T. Chatterjee, W.-L. Tsai, W.-K. Lee, M.-J. Wu, M. Jiao, K.-C. Pan, C.-L. Yi, C.-L. Chung, K.-T. Wong and C.-C. Wu, *Adv. Mater.*, 2016, **28**, 6976–6983.
- J. Mei, N. L. C. Leung, R. T. K. Kwok, J. W. Y. Lam and B. Z. Tang, *Chem. Rev.*, 2015, 115, 11718–11940.
- 6 S. D. Xu, T. T. Liu, Y. X. Mu, Y. F. Wang, Z. G. Chi, C. C. Lo, S. W. Liu, Y. Zhang, A. Lien and J. R. Xu, *Angew. Chem., Int. Ed.*, 2015, 54, 874–878.
- 7 (a) J. Huang, H. Nie, J. J. Zeng, Z. Y. Zhuang, S. F. Gan, Y. J. Cai, J. J. Guo, S.-J. Su, Z. J. Zhao and B. Z. Tang, Angew. Chem., Int. Ed., 2017, 56, 12971–12976; (b) J. J. Guo, X.-L. Li, H. Nie, W. Luo, R. Hu, A. Qin, Z. Zhao, S.-J. Su and B. Z. Tang, Chem. Mater., 2017, 29, 3623–3631.
- 8 (a) R. Furue, T. Nishimoto, I. S. Park, J. Lee and Y. Yasuda, Angew. Chem., Int. Ed., 2016, 55, 7171–7175; (b) L. Yu, Z. B. Wu, G. H. Xie, W. X. Zeng, D. G. Ma and C. L. Yang, Chem. Sci., 2018, 9, 1385–1391.
- 9 M. Aydemir, S. Xu, C. Chen, M. R. Bryce, Z. Chi and A. P. Monkman, *J. Phys. Chem. C*, 2017, **121**, 17764–17772.
- 10 T. Lu and F. W. Chen, J. Comput. Chem., 2012, 33, 580-592.
- 11 (a) B. He, W. Luo, S. Hu, B. Chen, S. Zhen, H. Nie, Z. J. Zhao and B. Z. Tang, J. Mater. Chem. C, 2017, 5, 12553–12560; (b) T. Han, H. Deng, Z. Qiu, Z. Zhao, H. Zhang, H. Zou, N. L. C. Leung, G. Shan, M. R. J. Elsegood, J. W. Y. Lam and B. Z. Tang, J. Am. Chem. Soc., 2018, 140, 5588–5598; (c) L. Chen, Y. -H. Wang, B. He, H. Nie, R. Hu, F. Huang, A. J. Qin, X. -S. Zhou, Z. J. Zhao and B. Z. Tang, Angew. Chem., Int. Ed., 2015, 54, 4231–4235; (d) H. Tsujimoto, D.-G. Ha, G. Markopoulos, H. S. Chae, M. A. Baldo and T. M. Swager, J. Am. Chem. Soc., 2017, 139, 4894–4900.
- 12 X.-L. Chen, J.-H. Jia, R. Yu, J.-Z. Liao, M.-X. Yang and C.-Z. Lu, *Angew. Chem., Int. Ed.*, 2017, **56**, 15006–15009.
- 13 A. Wakamiya, K. Mori and S. Yamaguchi, *Angew. Chem., Int. Ed.*, 2007, 46, 4273–4276.
- 14 (a) Z. Xie, C. Chen, S. Xu, J. Li, Y. Zhang, S. Liu, J. R. Xu and Z. G. Chi, *Angew. Chem., Int. Ed.*, 2015, 54, 7181–7184; (b) Z. L. Xie, Q. Y. Huang, T. Yu, L. Y. Wang, Z. Mao, W. L. Li, Z. Yang, Y. Zhang, S. W. Liu, J. R. Xu, Z. G. Chi and M. P. Aldred, *Adv. Funct. Mater.*, 2017, 27, 1703918.

- 15 Y. H. Lee, S. Park, J. Oh, J. W. Shin, J. Jung, S. Yoo and M. H. Lee, ACS Appl. Mater. Interfaces, 2017, 9, 24035–24042.
- 16 H. Wang, L. Xie, Q. Peng, L. Meng, Y. Wang, Y. Yi and P. Wang, Adv. Mater., 2014, 26, 5198–5204.
- 17 P. Rajamalli, N. Senthilkumar, P. Gandeepan, P.-Y. Huang, M.-J. Huang, C.-Z. R. Wu, C.-Y. Yang, M.-J. Chiu, L.-K. Chu, H.-W. Lin and C.-H. Cheng, *J. Am. Chem. Soc.*, 2016, **138**, 628–634.
- (a) J. S. Ward, R. S. Nobuyasu, M. A. Fox, A. S. Batsanov,
 J. Santos, F. B. Dias and M. R. Bryce, J. Org. Chem., 2018,
 83, 14431–14442; (b) J. S. Ward, R. S. Nobuyasu, M. A. Fox,
 J. A. Aguilar, D. Hall, A. S. Batsanov, Z. Ren, F. B. Dias and
 M. R. Bryce, J. Org. Chem., 2019, 84, 3801–3816.
- 19 G. A. Sommer, L. N. Mataranga-Popa, R. Czerwieniec, T. Hofbeck, H. H. Homeier, T. J. Müller and H. Yersin, J. Phys. Chem. Lett., 2018, 9, 3692–3697.
- 20 M. K. Etherington, J. Gibson, H. F. Higginbotham, T. J. Penfold and A. P. Monkman, *Nat. Commun.*, 2016, 7, 13680.
- 21 D.-H. Kim, A. D'Aléo, X.-K. Chen, A. D. S. Sandanayaka, D. Yao, L. Zhao, T. Komino, E. Zaborova, G. Canard, Y. Tsuchiya, E. Choi, J. W. Wu, F. Fages, J.-L. Brédas, J.-C. Ribierre and C. Adachi, *Nat. Photonics*, 2018, 12, 98–104.
- 22 X.-K. Chen, S.-F. Zhang, J.-X. Fan and A.-M. Ren, *J. Phys. Chem. C*, 2015, **119**, 9728–9733.
- 23 (a) Q. Zhang, J. Li, K. Shizu, S. Huang, S. Hirata, H. Miyazaki and C. Adachi, *J. Am. Chem. Soc.*, 2012, 134, 14706–14709; (b)
 Q. Zhang, T. Komino, S. Huang and C. Adachi, *Adv. Funct. Mater.*, 2012, 22, 2327–2336.
- 24 (a) J. Gibson, A. Monkman and T. Penfold, *ChemPhysChem*, 2016, 17, 2956–2961; (b) J. Gibson and T. Penfold, *Phys. Chem. Chem. Phys.*, 2017, 19, 8428–8434.
- 25 H. Noda, H. Nakanotani and C. Adachi, *Sci. Adv.*, 2018, 4, 6910.
- 26 H. F. Higginbotham, C.-L. Yi, A. P. Monkman and K.-T. Wong, *J. Phys. Chem. C*, 2018, **122**, 7627–7634.
- 27 (a) W.-L. Tsai, M.-H. Huang, W.-K. Lee, Y.-J. Hsu, K.-C. Pan, Y.-H. Huang, H.-C. Ting, M. Sarma, Y.-Y. Ho, H.-C. Hu, C.-C. Chen, M.-T. Lee, K.-T. Wong and C.-C. Wu, Chem. Commun., 2015, 51, 13662–13665; (b) T. Peng, G. Li, K. Ye, C. Wang, S. Zhao, Y. Liu, Z. Hou and Y. Wang, J. Mater. Chem. C, 2013, 1, 2920–2926; (c) S. Wu, S. Li, Q. Sun, C. Huang and M.-K. Fung, Sci. Rep., 2016, 6, 25821.
- 28 (a) J. W. Sun, J. H. Lee, C. K. Moon, K. H. Kim, H. Shin and J. J. Kim, Adv. Mater., 2014, 26, 5684–5688; (b) K. H. Kim, E. S. Ahn, J. S. Huh, Y. H. Kim and J. J. Kim, Chem. Mater., 2016, 28, 7505–7510; (c) S.-Y. Kim, W.-I. Jeong, C. Mayr, Y.-S. Park, K.-H. Kim, J.-H. Lee, C.-K. Moon, W. Brütting and J.-J. Kim, Adv. Funct. Mater., 2013, 23, 3896–3900.
- 29 Q. Q. Liang, C. M. Han, C. B. Duan and H. Xu, Adv. Opt. Mater., 2018, 6, 1800020.
- 30 W. H. Lee, D. H. Kim, P. J. Jesuraj, H. Hafeez, J. C. Lee, D. K. Choi, T.-S. Bae, S. M. Yu, M. Song, C. S. Kim and S. Y. Ryu, *Mater. Res. Express*, 2018, 5, 076201.
- 31 (a) S. Ying, D. Yang, X. Qiao, Y. Dai, Q. Sun, J. Chen, T. Ahamad, S. M. Alshehri and D. Ma, J. Mater. Chem. C, 2018, 6, 10793–10803; (b) C. Li, L. Duan, D. Zhang and Y. Qiu, ACS Appl. Mater. Interfaces, 2015, 7, 15154–15159.